Soft Matter

PAPER

View Article Online
View Journal | View Issue

Cite this: *Soft Matter*, 2018, **14**, 934

Energy landscapes for ellipsoids in non-uniform AC electric fields†

Isaac Torres-Díaz, Bradley Rupp, Yuguang Yang and Michael A. Bevan *

Received 20th November 2017,
Accepted 24th December 2017

DOI: 10.1039/c7sm02287e

rsc.li/soft-matter-journal

We report a closed-form analytical model for energy landscapes of ellipsoidal particles in non-uniform high-frequency AC electric fields to identify all possible particle positions and orientations. Three-dimensional equilibrium positions and orientations of prolate ($r_x = r_y < r_z$), oblate ($r_x = r_z > r_y$), and scalene ($r_x \neq r_y \neq r_z$) ellipsoids are reported *vs.* field frequency and amplitude, which are determined from energy landscape minima. For ellipsoids within non-uniform electric fields between co-planar parallel electrodes, the number of configurations of position and orientation is 6 for prolate, 5 for oblate, and 9 for scalene ellipsoids. In addition, for coplanar electrodes, conditions are identified when particles can be treated using a quasi-2D analysis in the plane of their most probable elevation near an underlying surface. The reported expressions are valid for time-averaged interactions of ellipsoid particles in arbitrary AC electric field configurations, such that our results are applicable to electromagnetic tweezers interacting with particles having an appropriate material property contrast with the medium in the frequency range of interest.

Introduction

The ability to manipulate the position and orientation of microscopic objects with external fields without direct mechanical intervention is an enabling capability for many aspects of nano- and micro-technologies. An important precedent is the use of electromagnetic radiation to manipulate colloidal particles in various forms including optical fields (*e.g.*, optical tweezers[1]), electric fields (*e.g.*, dielectrophoresis[2]), and magnetic fields (*e.g.*, magnetic tweezers[3,4]). A key aspect to all of these approaches is understanding very accurately how the applied field interacts with the object of interest. For example, understanding particle interactions with a focused laser beam is critical to designing and operating optical tweezer apparatus and optimizing for different particle material properties.[5] The same is true of manipulating magnetic particles with various magnetic field configurations.[6]

Here, we are concerned with ellipsoidal particles, having up to the three different axes (*i.e.*, tri-axial), interacting with non-uniform high frequency AC electric fields (Fig. 1). The ability to measure and model such particle–field interactions provides a basis to manipulate the position and orientation of anisotropic particles. Although a significant body of research has focused on transport of particles in AC electric fields,[7,8] which is referred to as dielectrophoresis, here we are specifically interested in the time-averaged interaction of induced dipoles with non-uniform AC electric fields. For example, previous work on spherical particles has shown how dipole-field interactions produce energy landscapes (energy *vs.* position) that dictate the forces, torques, and thermal sampling of particles about equilibrium positions located at either electric field maxima or minima at different field frequencies.[9–11]

For anisotropic colloidal particles, it is commonly understood that particles often align with their long-axis parallel to the dominant electric field direction during transport[7,8] and in concentrated systems.[12–15] However, it has also been known for some time, from at least two prior studies, that single uni-axial particles in AC electric fields can orient both parallel and perpendicular to field lines (for anisotropic cells).[16,17] The theory underlying this phenomena pre-dates these experimental observations,[18] but other than being used to capture frequency dependent cell orientations, it has not been used to model potential energy landscapes in colloidal systems with well-defined material properties. In particular, the authors are unaware of any previous studies that report the position and orientation dependent energy landscapes of anisotropic colloidal particles as a function of field frequency and amplitude.

In this work, we report closed-form energy landscapes for dielectric ellipsoids in non-uniform, high-frequency AC electric fields between coplanar electrodes (Fig. 1). Results are reported for prolate, oblate, and scalene ellipsoids as a function of field frequency and amplitude. In general, for scalene (*i.e.*, tri-axial) ellipsoids, net potential energy landscapes from superposition

Chemical & Biomolecular Engineering, Johns Hopkins University, Baltimore, MD 21218, USA. E-mail: mabevan@jhu.edu

† Electronic supplementary information (ESI) available. See DOI: 10.1039/c7sm02287e

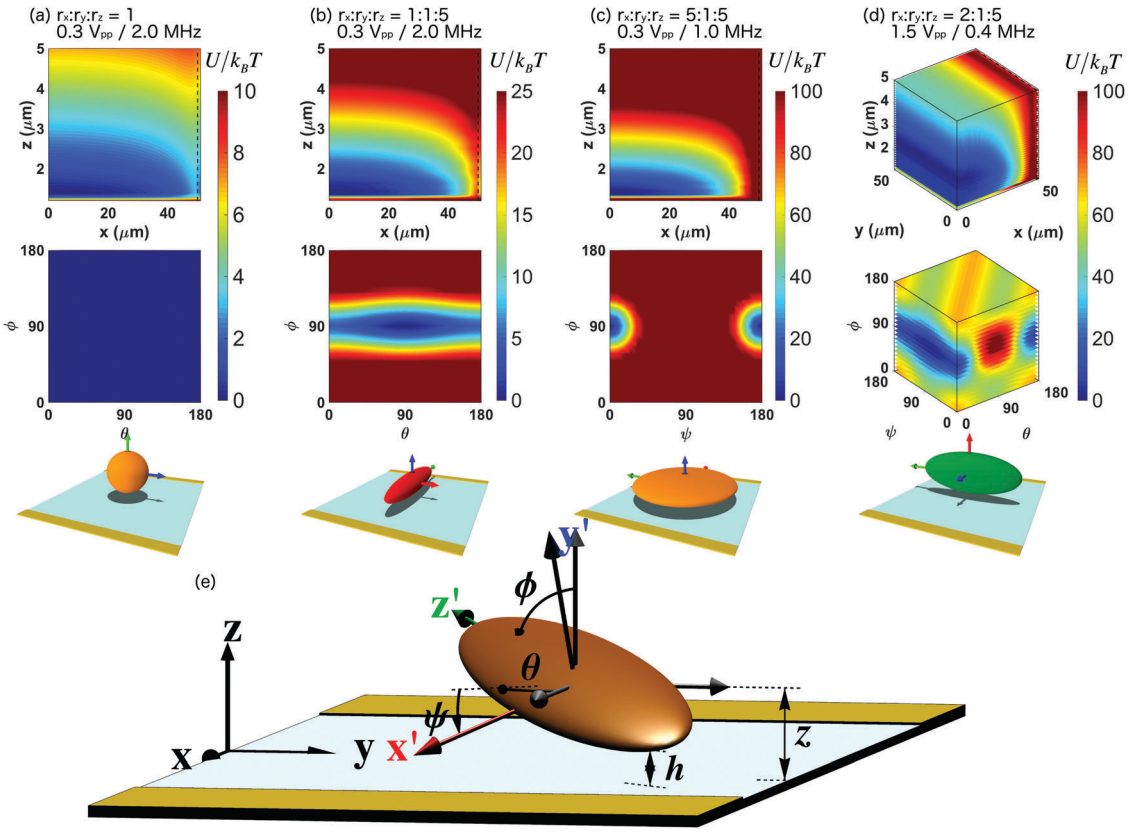

Fig. 1 Projected net potential energy for position and orientation of ellipsoids in non-uniform high-frequency AC electric fields between coplanar parallel electrodes (100 μm gap). (a) x–z and θ–ϕ projections for sphere ($r_x : r_y : r_z = 1$ μm) in 2 MHz 0.3 V_{pp} AC field. (b) x–z and θ–ϕ projections for prolate ellipsoid ($r_x : r_y : r_z = 1 : 1 : 5$ μm) in 2 MHz 0.3 V_{pp} AC field. (c) x–z and ψ–ϕ projections for oblate ellipsoid ($r_x : r_y : r_z = 5 : 1 : 5$ μm) in 1.0 MHz 0.3 V_{pp} AC field. (d) x–y–z and θ–ψ–ϕ projections for scalene ellipsoid ($r_x : r_y : r_z = 2 : 1 : 5$ μm) in 0.4 MHz 1.3 V_{pp} AC field. Equilibrium particle configuration (not to scale) is depicted at each condition. Particle x', y' and z' axes are represented as red, blue and green arrows. Material parameters are reported in Table 1. (d) Schematic of scalene ellipsoid arbitrarily orientated relative to coplanar parallel electrodes (not at scale) with orientation given by Euler angles (ϕ, θ, ψ). Colored primed coordinates attached to particle semi-axes are referred to as particle coordinates. Black unprimed coordinates attached to the planar surface are referred to as laboratory coordinates. Also labeled are the particle surface-wall minimum distance, h, and particle center elevation relative to the wall, z.

of substrate,[19] gravity, and electric field mediated interactions depend on six variables, with three for position and three for orientation as,

$$u^{\text{net}}(\mathbf{X}, \mathbf{\Theta}) = u^{\text{net}}(x, y, z, \theta, \phi, \psi), \quad (1)$$

where $\mathbf{X} = (x, y, z)$ represents the particle center of mass position, and $\mathbf{\Theta} = (\theta, \phi, \psi)$ the particle orientation. In contrast, the symmetry of prolate and oblate ellipsoids requires fewer orientation variables, and spheres have no orientation dependence. The present analysis of the time average potential energy landscapes for minimum energy states yields all available combinations of position and orientation for different field conditions and for different particle shapes. Results and findings include representative example energy landscapes, visual and plotted state diagrams of possible states, and an analysis of conditions where quasi-two dimensional behavior is a reasonable approximation of the six dimensional dependence in eqn (1). The theoretical potentials presented in this work are general to other electrode configurations and should be extensible to describe particle–field potentials and orientations in concentrated systems.

Theory

Laboratory & particle coordinates

Consider an ellipsoidal colloidal particle near a planar surface (Fig. 1(e)). The colloid is under the influence of a non-uniform AC electric field generated between parallel thin electrodes of negligible thickness. The ellipsoid principal semi-axes (r_x, r_y, r_z) are directed along the x', y', and z' axes, which is the particle frame. The unprimed axes x, y, and z represent the laboratory coordinates with origin between the symmetry plane electrode gap center. The relative orientation of the particle is defined by the Euler angles (θ, ϕ, ψ), where ϕ represents the polar angle, θ the azimuthal angle, and ψ the rotation angle around the z' axis. The variable x represents the particle position relative to the electrode gap center, z is the elevation of the particle center relative the planar wall surface, and h represents the distance of closest

approach between the particle and wall. In the following, it will be shown how to relate variables in the laboratory (x, y, z) and particle (x', y', z') frames by a rotation transformation matrix.

Net potential energy landscape

The net potential energy of a particle near a planar wall (Fig. 1(e)) under the influence of an AC electric field is given by particle–wall (pw) and particle–field (pf) interactions

$$u^{\text{net}}(\mathbf{X}, \mathbf{\Theta}) = u^{\text{pw}}(\mathbf{X}, \mathbf{\Theta}) + u^{\text{pf}}(\mathbf{X}, \mathbf{\Theta}), \tag{2}$$

where $\mathbf{X} = (x, y, z)$ and $\mathbf{\Theta} = (\theta, \phi, \psi)$. In this work, due to the symmetry of electrodes, there is no dependence in the y-direction. For axisymmetric particles, like prolate ($r_x = r_y < r_z$) and oblate ($r_x = r_z > r_y$) ellipsoids, the net potential energy does not depend on the angle ψ and θ, respectively (Fig. 1). For uniform spherical particles, the angular dependence vanishes.[10] The present study is concerned only with particles within the non-uniform electric field between electrodes, so that particle-electrode interactions are not considered.

Particle–wall potential

The particle–wall potential allows particles to sample different positions and orientations without touching the substrate. Particle–wall interactions are considered to be dominated by electrostatic repulsion with a negligible van der Waals contribution. The net particle–wall interaction energy is given by electrostatic interaction[19–21]

$$u^{\text{pw}}(z, \phi, \theta, \psi) = \frac{Z \exp(-\kappa h)}{\sqrt{\Gamma}}, \tag{3}$$

$$Z = 64\pi\varepsilon_{\text{m}}\left(\frac{k_{\text{B}}T}{z_{\text{v}}e}\right)^2 \tanh\left(\frac{z_{\text{v}}e\psi_{\text{p}}}{4k_{\text{B}}T}\right)\tanh\left(\frac{z_{\text{v}}e\psi_{\text{w}}}{4k_{\text{B}}T}\right), \tag{4}$$

where κ^{-1} is the Debye length, ε_{m} is the medium dielectric constant, k_{B} is Boltzmann's constant, T is the absolute temperature, e is the electron charge, z_{v} is electrolyte valence, and ψ_{p} and ψ_{w} are particle and wall surface potentials. Γ is the Gaussian curvature of the particle where the distance between surfaces, h, is minimum. For ellipsoidal particles, h is function of both particle position and orientation, and Γ is a function only of the relative particle orientation given by[19]

$$h(z, \phi, \theta, \psi) = z - \sqrt{(r_x A_{13})^2 + (r_y A_{23})^2 + (r_z A_{33})^2},$$

$$\Gamma(\phi, \theta, \psi) = \frac{\left[(r_x A_{13})^2 + (r_y A_{23})^2 + (r_z A_{33})^2\right]^2}{r_x^2 r_y^2 r_z^2},$$

$$A_{13} = \sin\psi\sin\phi, \quad A_{23} = \cos\psi\sin\phi, \quad A_{33} = \cos\phi. \tag{5}$$

Particle–field potentials

The net particle–field interaction includes the gravitational potential energy and the interaction of the induced dipole with the applied electric field given by superposition as

$$u^{\text{pf}}(\mathbf{X}, \mathbf{\Theta}) = u_{\text{g}}^{\text{pf}}(z) + u_{\text{de}}^{\text{pf}}(\mathbf{X}, \mathbf{\Theta}), \tag{6}$$

where the gravitational potential energy relative to the substrate is given by

$$u_{\text{g}}^{\text{pf}}(z) = v_{\text{p}}(\rho_{\text{p}} - \rho_{\text{m}})gz, \tag{7}$$

where $v_{\text{p}} = 4\pi r_x r_y r_z/3$ is the particle volume, g is acceleration due to gravity, ρ_{p} and ρ_{m} are the particle and medium densities. For a dielectric ellipsoidal particle, the interaction energy between the induced dipole and the applied electric field is[18]

$$u_{\text{de}}^{\text{pf}} = -k_{\text{B}}T\lambda\sum_{i=1}^{3}\left[\frac{f_{\text{CM},i}}{|f_0|^2}\left(E_i^{*\prime}\right)^2\right], \tag{8}$$

$$\lambda \equiv (3/4)(\varepsilon_{\text{m}}v_{\text{p}}/k_{\text{B}}T)|f_0|^2(E_0^{*})^2, \tag{9}$$

where λ is a dimensionless ratio of the magnitude of the time-average induced dipole–field interaction energy and the thermal energy. The index i = 1, 2, 3 (x', y', z') represents the particle principal axes, $f_{\text{CM},i}$ is the Clausius–Mossotti factor along the particle's i-axis, and f_0 is the f_{CM} of the shortest axis at zero frequency. The f_{CM} along the i-axis of the particle is defined by[18]

$$f_{\text{CM},i} = \text{Re}\left[\frac{1}{3}\frac{\tilde{\varepsilon}_{\text{p},i} - \tilde{\varepsilon}_{\text{m}}}{\tilde{\varepsilon}_{\text{m}} + (\tilde{\varepsilon}_{\text{p},i} - \tilde{\varepsilon}_{\text{m}})L_i}\right], \tag{10}$$

where $\tilde{\varepsilon}_{\text{m}}$ is the complex medium permittivity, $\tilde{\varepsilon}_{\text{p},i}$ is the complex particle permittivity along the i-axis of the particle. Both are expressed as $\tilde{\varepsilon} = \varepsilon - i\sigma/\omega$, where σ is conductivity, and ω is the electric field frequency. L_i is a parameter defined in the solution of Laplace's equation in ellipsoidal coordinates, which quantifies the anisotropy of the particle along the i-axis[18]

$$L_i = \frac{r_x r_y r_z}{2}\int_0^\infty \frac{\text{d}\alpha}{(\alpha + r_i^2)\sqrt{(\alpha + r_x^2)(\alpha + r_y^2)(\alpha + r_z^2)}}. \tag{11}$$

In eqn (9), $E_i^{*\prime} = E_i'/(V_{\text{pp}}/\pi d_{\text{g}})$ is the normalized electric field in the direction of the i-axis of the particle, where $V_{\text{pp}} = 2V_0$ is the peak-to-peak voltage, and d_g is the electrode gap. The electric field in the particle coordinates $\mathbf{E}'$ is related to the field in laboratory coordinates $\mathbf{E}$ by

$$\mathbf{E}' = \mathbf{A}\cdot\mathbf{E}, \tag{12}$$

where the rotation transformation matrix $\mathbf{A}$ is defined by

$$\mathbf{A} = \begin{pmatrix} A_{11} & A_{12} & A_{13} \\ A_{21} & A_{22} & A_{23} \\ A_{31} & A_{32} & A_{33} \end{pmatrix} = \begin{pmatrix} \cos\psi\cos\theta - \cos\phi\sin\theta\sin\psi & \cos\psi\sin\theta + \cos\phi\cos\theta\sin\psi & \sin\psi\sin\phi \\ -\sin\psi\cos\theta - \cos\phi\sin\theta\cos\psi & -\sin\psi\sin\theta + \cos\phi\cos\theta\cos\psi & \cos\psi\sin\phi \\ \sin\phi\sin\theta & -\sin\phi\cos\theta & \cos\phi \end{pmatrix} \tag{13}$$

where in the present work, we use Euler angles, although an alternative way to describe this system is using quaternion parameters (e_0, e_1, e_2, e_3).[22] The electric field, **E**, between coplanar electrodes is[23]

$$E_x = \frac{2V_0}{\pi d}\left[\tan^{-1}\left(\frac{\sin\hat{x}}{\sinh\hat{z}}\right) - \tan^{-1}\left(\frac{\cos\hat{x}}{\sinh\hat{z}}\right)\right],$$
$$E_z = \frac{V_0}{\pi d}\left[\ln\left(\frac{\cosh\hat{z}+\cos\hat{x}\cosh\hat{z}+\sin\hat{x}}{\cosh\hat{z}-\cos\hat{x}\cosh\hat{z}-\sin\hat{x}}\right)\right], \quad (14)$$

where $\hat{x} = \pi(x + d)/2d + \pi/4$ and $\hat{z} = \pi z/2d$, where d is the electrode gap. In eqn (8), the electric field can be expressed in normalized form as $\mathbf{E}^* = \mathbf{E}/(V_{pp}/\pi d)$.

Probability distributions & potentials

For particles near infinite dilution, the probability $p(\mathbf{X}, \mathbf{\Theta}) = p(x, y, z, \phi, \theta, \psi)$ of sampling different positions and orientations is related to potential energy by Boltzmann's equation as

$$p(\mathbf{X}, \mathbf{\Theta}) = p(\mathbf{X}_r, \mathbf{\Theta}_r)\exp[-(u^{net}(\mathbf{X}, \mathbf{\Theta}) - u^{net}(\mathbf{X}_r, \mathbf{\Theta}_r))/k_BT], \quad (15)$$

where $u^{net}(\mathbf{X}, \mathbf{\Theta})$ is the net potential energy in eqn (2), and $\mathbf{X}_r$ and $\mathbf{\Theta}_r$ are the reference position and orientation in the relative potential energy. Since the net potential energy of the anisotropic particle has a dependence on six variables, it is necessary to reduce the dimensionality of probability distributions and potentials for visualization and comparison with experimental data. The angle-averaged distribution $\langle p(\mathbf{X})\rangle_{\mathbf{\Theta}}$ can be calculated by[24]

$$\langle p(\mathbf{X})\rangle_{\mathbf{\Theta}} = \int_{\psi_i}^{\psi_f}\int_{\phi_i}^{\phi_f}\int_{\theta_i}^{\theta_f} p(x,y,z,\phi,\theta,\psi)\sin\phi\,d\theta\,d\phi\,d\psi \Big/ \int_{\psi_i}^{\psi_f}\int_{\phi_i}^{\phi_f}\int_{\theta_i}^{\theta_f}\sin\phi\,d\theta\,d\phi\,d\psi, \quad (16)$$

where the integration limits are 0 and 180 degrees due to particles' orientational symmetry. Eqn (16) can be used to determine the effective position dependent, or angle-averaged, potential $\langle u^{net}(\mathbf{X})\rangle_{\mathbf{\Theta}}$ *via* an inverse Boltzmann's relation as

$$\frac{\langle u^{net}(\mathbf{X})\rangle_{\mathbf{\Theta}} - \langle u^{net}(\mathbf{X}_r)\rangle_{\mathbf{\Theta}}}{k_BT} = \ln\left[\langle p(\mathbf{X}_r)\rangle_{\mathbf{\Theta}}/\langle p(\mathbf{X})\rangle_{\mathbf{\Theta}}\right]. \quad (17)$$

and, in a similar way, the position-averaged distribution $\langle p(\mathbf{\Theta})\rangle_{\mathbf{X}}$ can be calculated by

$$\langle p(\mathbf{\Theta})\rangle_{\mathbf{X}} = \frac{1}{(z_f - z_i)(y_f - y_i)(x_f - x_i)}\int_{z_i}^{z_f}\int_{y_i}^{y_f}\int_{x_i}^{x_f} p(x,y,z,\phi,\theta,\psi)\,dx\,dy\,dz, \quad (18)$$

where the integration limits in x and y are defined by the electrode geometry and z must be greater than the longest particle axis. Eqn (18) can be used to determine the effective orientation dependent, or position-averaged potential $\langle u^{net}(\mathbf{\Theta})\rangle_{\mathbf{X}}$ as a function particle orientation as

$$\frac{\langle u^{net}(\mathbf{\Theta})\rangle_{\mathbf{X}} - \langle u^{net}(\mathbf{\Theta}_r)\rangle_{\mathbf{X}}}{k_BT} = \ln\left[\langle p(\mathbf{\Theta}_r)\rangle_{\mathbf{X}}/\langle p(\mathbf{\Theta})\rangle_{\mathbf{X}}\right]. \quad (19)$$

Another lower-dimensional case of interest is the quasi-2D distribution of states projected onto a surface, which is often the case with optical microscopy measurements.[25–27] For the position, x, and orientation angle, θ, of the particle, the average probability is expressed as

$$\langle p(x,\theta)\rangle_{y,z,\phi,\psi} = \frac{\int_{z_i}^{z_f}\int_{y_i}^{y_f}\int_{\phi_i}^{\phi_f}\int_{\psi_i}^{\psi_f} p(x,y,z,\phi,\theta,\psi)\,dz\,dy\,d\phi\,d\psi}{(z_f - z_i)(y_f - y_i)(\phi_f - \phi_i)(\psi_f - \psi_i)}, \quad (20)$$

which can be used to calculate the effective projected potential $\langle u^{net}(x,\theta)\rangle_{y,z,\phi,\psi}$ by

$$\frac{\langle u^{net}(x,\theta)\rangle_{y,z,\phi,\psi} - \langle u^{net}(x_r,\theta_r)\rangle_{y,z,\phi,\psi}}{k_BT} = \ln\left[\langle p(x_r,\theta_r)\rangle_{y,z,\phi,\psi}\Big/\langle p(x,\theta)\rangle_{y,z,\phi,\psi}\right]. \quad (21)$$

Quasi-2D analysis

In the following, an estimate is provided for the maximum applied voltage when a quasi-2D analysis is appropriate. For a particle at the middle of the gap at a fixed orientation parallel to the x-component of the field, the net potential energy of the particle (eqn (2)) reduces to

$$\frac{u^{net}(z)}{k_BT} = B_e\frac{\exp(-\kappa h)}{\sqrt{r_m^2\Gamma}} + G\frac{z}{r_m} - 4\lambda\frac{f_{cm,i}}{|f_0|^2}\tan^{-1}\left(\frac{1}{\sqrt{2}}\mathrm{csch}\left(\frac{\pi z}{2d}\right)\right)^2, \quad (22)$$

where $G \equiv \nu_p(\rho_p - \rho_m)gr_m/k_BT$, $B_e \equiv Zr_m/k_BT$, and r_m is the minimum semi-axis length of the particle. Eqn (22) shows that in the middle of the gap at a fixed orientation, the equilibrium position is determined by a balance between gravity, electrostatic repulsion, and the gradient of the x-component of the field along the z-axis. For conditions where the particle is not close to the surface where electrostatic interactions are negligible, the minimum energy state (where the gradient of eqn (22) vanishes) yields the maximum ratio between electrical and gravitational energy required for quasi-2D behavior as

$$\frac{\lambda}{G} = \frac{1}{4}\left|\frac{f_0^2}{f_{cm,i}}\right|\frac{\sqrt{2}}{\pi^2}\frac{d_g}{r_m}\frac{d_g}{d_g - 2z}, \quad (23)$$

which upon further simplification after inserting λ and G yields the maximum applied voltage as

$$V_{pp,max} = \pi d_g\sqrt{\frac{\sqrt{2}}{\pi^2}\frac{(\rho_p - \rho_m)g}{3\varepsilon_m}\frac{d_g}{|f_{cm,i}|}\left(\frac{d_g}{d_g - 2z}\right)}, \quad (24)$$

where in eqn (23) and (24) the analytical form is simplified *via* the following approximation

$$\frac{d}{dz}\left[\tan^{-1}\left(\frac{1}{\sqrt{2}}\mathrm{csch}\left(\frac{\pi z}{2d_g}\right)\right)^2\right] \approx \frac{\pi^2}{\sqrt{2}d_g}\left(1 - \frac{2z}{d_g}\right) \quad (25)$$

Since eqn (24) is an estimated value of the maximum voltage for a quasi-2D analysis, the position of the particle can be evaluated as the axis length perpendicular to the wall (*e.g.*, $z = r_x$).

Results & discussion

Particle shapes & physical parameters

The equilibrium position and orientation of ellipsoidal particles are investigated in non-uniform AC electric fields for different aspect ratios and typical material properties (Table 1). We consider three representative particle shapes with aspect ratios of: (a) $r_x : r_y : r_z$ = 1 : 1 : 5 μm (prolate), (b) 5 : 1 : 5 μm (oblate), and (c) 2 : 1 : 5 μm (scalene). The particle and medium dielectric constants were fixed to $\varepsilon_m = 78\varepsilon_0$ and $\varepsilon_p = 3.2\varepsilon_0$, which are typical values reported for water and polymer colloids (*e.g.*, SU8 photoresist particles). The conductivities along different axes for each ellipsoid type in Table 1 are motivated by parameters identified in preliminary experimental results (unpublished). Finally, in an initial parametric search, the medium conductivity was systematically varied from 1 to 10 μS cm^{-1} (while fixing all other properties) to identify conditions for the maximum number of states for each case, which produced the medium conductivities in Table 1. The material parameters reported in Table 1 are realistic for dielectric particles in low ionic strength aqueous media and are useful for analyzing how f_{CM} along different particle axes influence equilibrium positions and orientations *vs.* field frequency and amplitude.

Fig. 2 shows the f_{CM} for the principal axes of the ellipsoidal particles as a function of medium conductivity and AC field frequency. Due to the shape anisotropy, the f_{CM} associated with different particle axes have different crossover frequencies. Fig. 2 shows the interval of crossover frequencies is shorter as the conductivity of the surrounding medium increases. For isotropic spherical particles, the three axes have the same f_{CM} with the same crossover frequency.[7] In the following, we show the conditions that generate a greater number of positions and orientations between the parallel electrodes as a function of the field frequency.

Energy landscape for prolate ellipsoids

Prolate particles have symmetry along the z'-axis, which eliminates any ψ-angle dependence. Since the y-component of the field is zero there is no dependence along that coordinate. In Fig. 3, results are shown for the projected 2D position (x, z) and orientation (θ, ϕ) energy landscapes (eqn (2), (17) and (19)) for a prolate particle ($r_x : r_y : r_z$ = 1 : 1 : 5 μm) at four different field

Table 1 Properties of media and ellipsoids investigated in this study. For each aspect ratio, columns report surface conductivities of each particle axis as well as the medium conductivity. The medium and particle dielectric constants in call cases are $\varepsilon_m = 78\varepsilon_0$ and $\varepsilon_p = 3.2\varepsilon_0$

Shape	$r_x : r_y : r_z$	σ_x (μS cm^{-1})	σ_y (μS cm^{-1})	σ_z (μS cm^{-1})	σ_m (μS cm^{-1})
Prolate	1 : 1 : 5	20	20	40	3
Oblate	5 : 1 : 5	30	10	30	1
Scalene	2 : 1 : 5	20	12	26	2

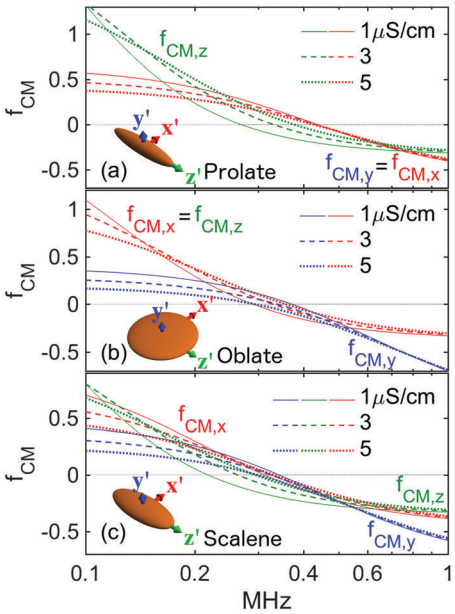

Fig. 2 Clausius–Mossotti factors, f_{CM}, for principal axes of ellipsoids *vs.* electric field frequency and medium conductivity (see inset legends). The particle aspect ratios are $r_x : r_y : r_z$ = (a) 1 : 1 : 5 μm, (b) 5 : 1 : 5 μm, and (c) 2 : 1 : 5 μm, which are depicted in the panel insets. Material parameters are in Table 1.

conditions, and the renderings for the minimum energy landscape. For field conditions of 100 kHz and 0.3 V_{pp}, Fig. 3(a), the minimum of the projected energy landscape indicates that the equilibrium state of the particle center is located close to the edge of the electrode gap, as in the case of spherical particles.[10] However, due to the particle aspect ratio, the projected energy landscape of the particle position possesses three relative energy minima at different elevations (Fig. 3(a)). These energy minima are not reflected in the orientational projection of the energy landscape, where it is shown that the long axis of the particle is oriented parallel to the field x-component. This corresponds to the configuration shown in red in the bottom rendering.

For field conditions of 300 kHz and 0.3 V_{pp}, Fig. 3(b) shows the positional and orientational projections of the energy landscape, which indicate that the equilibrium state of the particle center is located close to the edge of the electrode gap, and the long axis is perpendicular to the field x-component. Here, the minimum appears at $\theta = 0^\circ$ or 180°, indicating that the z'-axis of the particle could be oriented along the positive or negative y-direction in the laboratory coordinates. The change in the particle orientation between 100 and 300 kHz is correlated with the crossover frequency between the f_{CM} along the long axis (z-axis) and short axis (x-axis), as depicted in Fig. 2. Again, this effect is not seen in spheres[10] since they are isotropic.

For a further frequency increase, at 500 kHz and 0.3 V_{pp}, the minimum of the positional and orientational projections of the energy landscape indicate that the equilibrium state of the particle keeps the same orientation as for 300 kHz, but it is now located in the middle of the electrode gap as shown in Fig. 3(c). Here, the transition between the particle position at the edge of

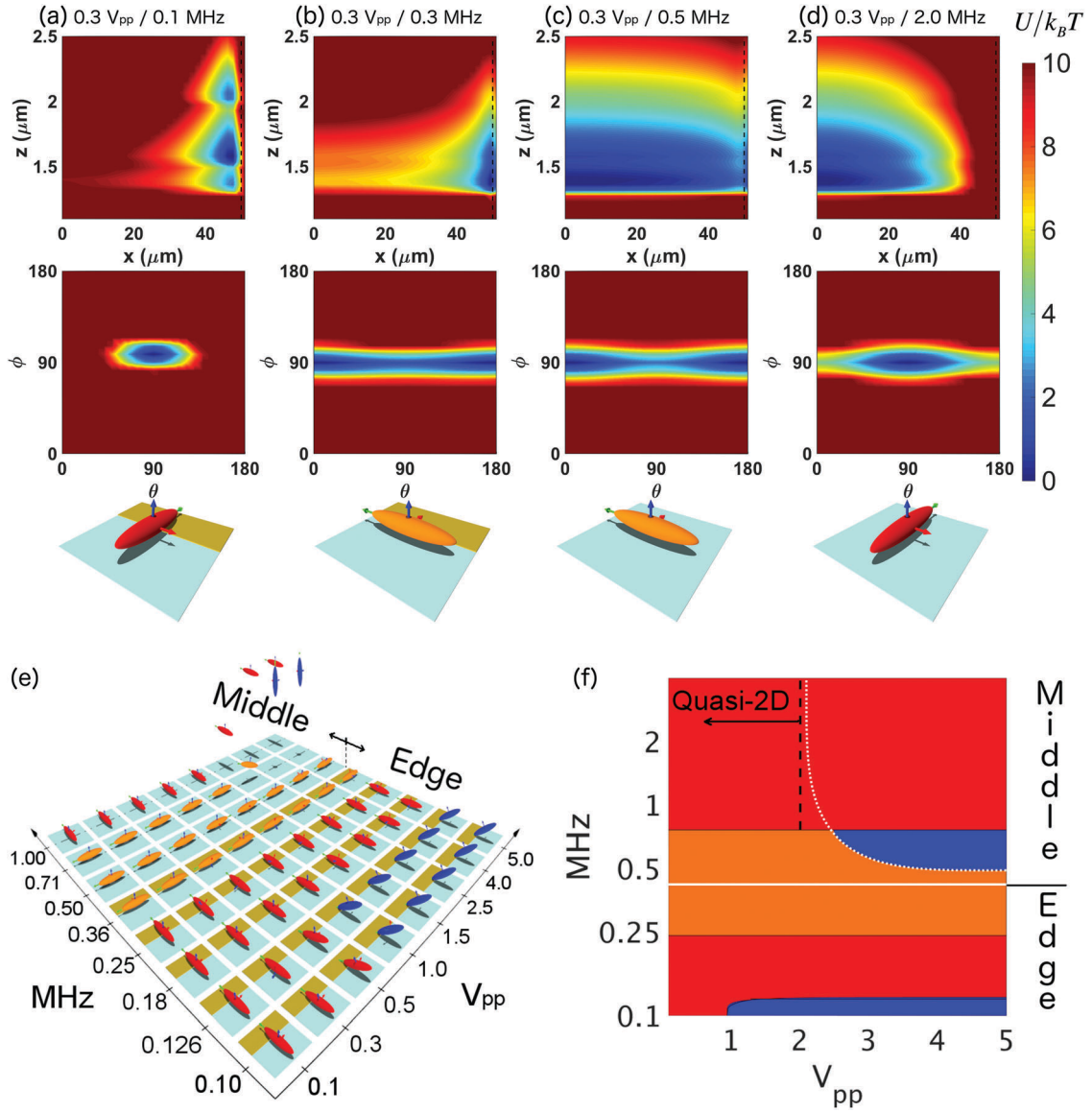

Fig. 3 Position and orientation projected energy landscapes for prolate ellipsoids ($r_x : r_y : r_z$ = 1 : 1 : 5) from 0–10k_BT relative to the global energy minimum. Field conditions are for 0.3 V_{pp}, and frequencies of (a) 0.1, (b) 0.3, (c) 0.5, and (d) 2 MHz. The lowest energy state is rendered under energy landscape plots. Material parameters are listed in Table 1. (e) Discrete rendered states *vs.* voltage and frequency category axes. (f) Continuous state diagram *vs.* field strength and frequency. Solid white line indicates the transition in position from the electrode edges to electrode center. Dashed white line indicates when particles move away from the surface. Dashed black line is maximum V for quasi-2D analysis (eqn (24)).

the electrode gap (300 kHz) and in the middle of the electrode gap (500 kHz) is correlated with the change in the sign of the f_{CM} as shown in Fig. 2(a). In the two first cases in Fig. 3(a) and (b) the value of f_{CM} is positive, indicating that the particle is more polarizable that the surrounding medium, and it is located at the electric field maximum. In contrast, at 500 kHz, the particle is less polarizable than the surrounding medium and is located at the electric field minimum. At still higher frequencies, 2 MHz and 0.3 V_{pp}, the Fig. 3(d) shows that the particle is still in the middle of the electrode gap since the f_{CM} is negative, and the long axis is oriented along the x-component of the electric field. The change in orientation between 500 kHz and 1 MHz is correlated with the crossover frequency between the f_{CM} of the short and long axes, as seen in Fig. 2(a). It determines which axis is aligned with the electric field.

To understand the orientation of single prolate particles in a non-uniform electric field, we calculated the minimum of the energy landscape at different applied voltages. Fig. S1 (ESI†) shows the equilibrium position and orientation of a prolate particle at different medium conductivity values as a function of the voltage and frequency of the applied field. It is seen that as the medium conductivity increases, *i.e.* the difference between particle and medium conductivities decreases, the particle can reach perpendicular position at the edge of the electrode at high voltages, *i.e.* there is a change in the absolute minimum as shown in Fig. 3(a). However, its equilibrium position is shifted

towards the middle of the electrode gap. Additionally, for greater medium conductivity values, the range of crossover frequencies between different orientations decreases and the particle reaches fewer configurations at different field conditions.

Results in Fig. S1(b) (ESI†) yield the position/orientation state diagram for the prolate particle (Fig. 3(f)). Some representative conditions are depicted in Fig. 3(e). In Fig. 3(f), the black dashed line corresponds with the approximated conditions (eqn (24)) that limits the quasi-2D analysis, *i.e.* when the long axis of the particle is parallel to the substrate. The white dotted line corresponds to the calculated conditions where the particle moves away from the substrate. Here, it is seen that the prolate particle can be controlled in a quasi-2D conditions at low voltages, and in three-dimensional space at higher voltages. From Fig. S1 (ESI†), it is seen that the number of states for a prolate particle can change depending of the particle and medium properties, *i.e.* depending of the f_{CM} along the particle axes. It is seen that a prolate ellipsoid ($r_x : r_y : r_z = 1 : 1 : 5$ μm) can reach the maximum number of six states by varying the field amplitude and frequency. The six total configurations include three at the electrode gap middle and three at the electrode edge. The prolate ellipsoid long axis can be oriented parallel and perpendicular to the field direction, and at higher field strengths it can also be aligned perpendicular to the wall.

Energy landscape for oblate ellipsoids

A similar analysis to that for the prolate particle in Fig. 3 has been conducted to understand the behavior of oblate particles ($r_x : r_y : r_z = 5 : 1 : 5$ μm). It has symmetry along the y'-axis, and as shown in Fig. 1, the energy landscape has no dependence on the θ-angle. In Fig. 4, we show the results for the projected 2D position (x, z) and orientation (ψ, ϕ) energy landscapes (eqn (2), (17) and (19)) for an oblate particle at four different field conditions, where the particle configuration at the minimum energy landscape for each condition is depicted at the bottom.

For 0.3 V_{pp}, the particle has two different positions at the edge and in the middle of the electrode gap. The first condition is at low frequencies where f_{CM} is positive (Fig. 2(b)); *i.e.* that particle is more polarizable than the surrounding medium, and it is located at the electric field maximum. At higher field frequencies, where f_{CM} is negative (Fig. 2(b)), the particle is located in the middle of the electrode gap where the field is minimum. Due to the symmetry of the oblate particle along the y'-axis, it behaves similar to a spherical particle, when the short axis is perpendicular to the substrate. Even though that under these conditions the particle is oriented parallel to the wall, there is a small variation in the location of the energy landscape minimum, and the local gradient around it, as shown in Fig. 4(a)–(d). However, it is clear that this particle shape can be analyzed in quasi-2D conditions at low field strengths.

The oblate particle behavior has been characterized at different medium conductivities and field strengths. Fig. 4(f) shows the conditions for a large number of states where its properties are listed on Table 1. It is shown the equilibrium state configuration as a state diagram as a function of the field frequency and voltage, and some representative states are depicted in Fig. 4(e). In Fig. 4(f), the black dashed line corresponds to the conditions (eqn (24)) that can be approximated by the quasi-2D analysis, *i.e.* when the short axis of the particle is perpendicular to the substrate. The white dotted line corresponds to the limit where the particle moves away from the substrate, and it describes the required conditions for a three-dimensional control on the particle.

It is seen that the short axis of a particle with oblate shape ($r_x : r_y : r_z = 5 : 1 : 5$ μm) is preferentially aligned perpendicular to the wall at low voltages. It can reach five different states at different field amplitude and frequency conditions. When the short axis of the particle is perpendicular (y-direction) to the field direction, the particle energy along the z-axis overcomes the gravitational energy making the particle moves away from the substrate. Interestingly, the frequency when the oblate particle moves from the edge to the middle of the electrode gap is dependent on the magnitude of the field strength. This is a result of the different crossover frequencies of the particle axes in Fig. 2(b). The short axis of the particle is less polarizable the medium, while the long axis still being more polarizable than the medium. For this case at high voltages, the dipole–field interaction energy overcomes gravitational energy, and the short axis is aligned with the field x-component, thus determining the equilibrium position. The orientation of oblate-like particles with different electric field conditions has been reported,[28] where the short axis of the plate-like particles is oriented parallel to the wall and perpendicular to the main component of the field. The present study shows the required and necessary conditions to control the position and orientation of such oblate particles at different field conditions.

Energy landscape for scalene ellipsoids

Before describing the net potential energy landscape for scalene ellipsoids, the possible states are discussed for tri-axial particles at different field conditions. For a given field frequency, the net potential energy for anisotropic particles depends on position and orientation. To describe the equilibrium particle state, Fig. S2 (ESI†) schematically depicts different particle configurations at the electrode edge where positional and orientational coordinates are plotted separately. Fig. S2(a) (ESI†) illustrates the most probable position of the particle center in the vicinity of the energy landscape minimum in each case and its projections onto different spatial planes. Similarly, Fig. S2(b) (ESI†) illustrates the most probable orientations of particle in the vicinity of the energy landscape minimum in each case including projections. Here, we show only the angular variation between 0 and 180°, since the ellipsoidal particle has three perpendicular planes of symmetry.[29] The states in Fig. S2(a) and (b) (ESI†) are color coded according the rendered configurations in Fig. S2(c) (ESI†).

The six different possible configurations in Fig. S2(c) (ESI†) are different from previous predictions for scalene anisotropic particles, which have shown that particles could only be oriented along the three principal axes.[16,17,30] The main difference is that the field generated in the parallel electrode configuration has components in the x- and z-directions, which increases the possible particle configurations. For scalene particles, the maximum number of possible orientational states is equal to the product

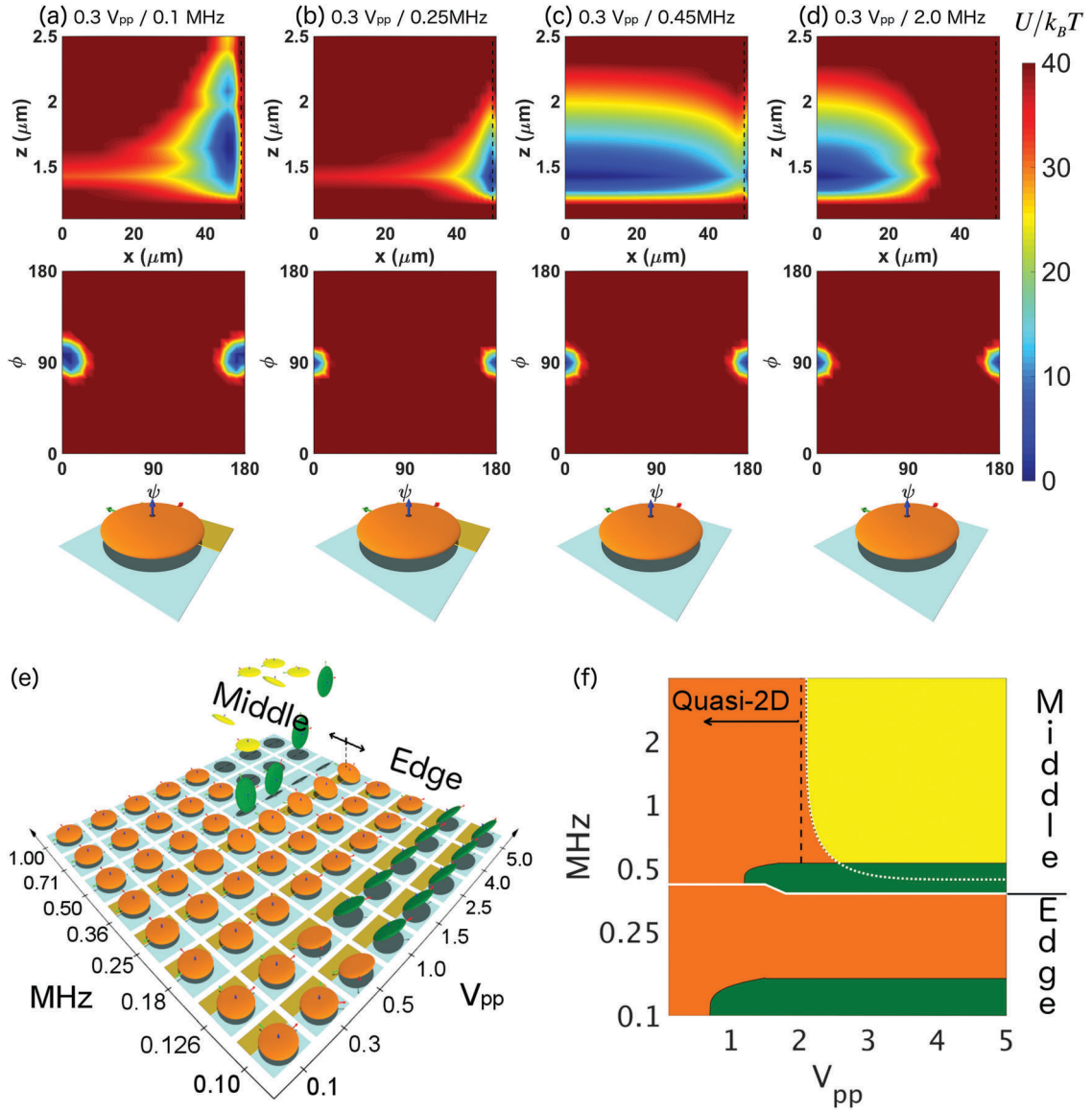

Fig. 4 Position and orientation projected energy landscapes for oblate ellipsoids ($r_x:r_y:r_z$ = 5 : 1 : 5) from 0–100 k_BT relative to the global energy minimum. Field conditions are for 0.3 V_{pp}, and frequencies of (a) 0.1, (b) 0.25, (c) 0.45, and (d) 1 MHz. The lowest energy state is rendered under energy landscape plots. Material parameters are listed in Table 1. (e) Discrete rendered states *vs.* voltage and frequency category axes. (f) Continuous state diagram *vs.* field strength and frequency. Solid white line indicates the transition in position from the electrode edges to electrode center. Dashed white line indicates when particles move away from the surface. Dashed black line is maximum *V* for quasi-2D analysis (eqn (24)).

of the number of field components and the number of different axes of the particle. Due to the symmetry of prolate and oblate particles, the maximum number states at the electrode is three, and of course, spheres have a single state because of their isotropic shape. The states in Fig. S2(c) (ESI†) are also possible at the center of the electrode gap. We use the same color scheme to define particle's orientational configurations whether they are at the electrode edge or electrode gap center. Based on this information, a scalene particle can be positioned and oriented in a maximum of twelve different states between parallel electrodes.

In Fig. 5, results are shown for the projected 3D position and orientation energy landscapes (eqn (2), (17) and (19)) for a scalene particle ($r_x:r_y:r_z$ = 2 : 1 : 5 μm) at four different field conditions. In this case, there is no rotational symmetry along any particle axis, so position and orientation averaged energy landscapes cannot be shown as 2D surfaces. Each case must consider three spatial and orientational axes for each case. Even though there is no field gradient along the *y*-axis, the orientation averaged energy landscape in a three dimensional space is plotted to show the generality of the analysis, which can be applied to any other electrode configuration. For field conditions of 100 kHz and 0.3 V_{pp} (λ = 0.8), Fig. 5(a) shows that the minimum of the projected energy landscape indicates that the equilibrium state of the particle center is located close to the edge of the electrode gap, as in the case of spherical particles.[10] Under these conditions, the position averaged energy landscape

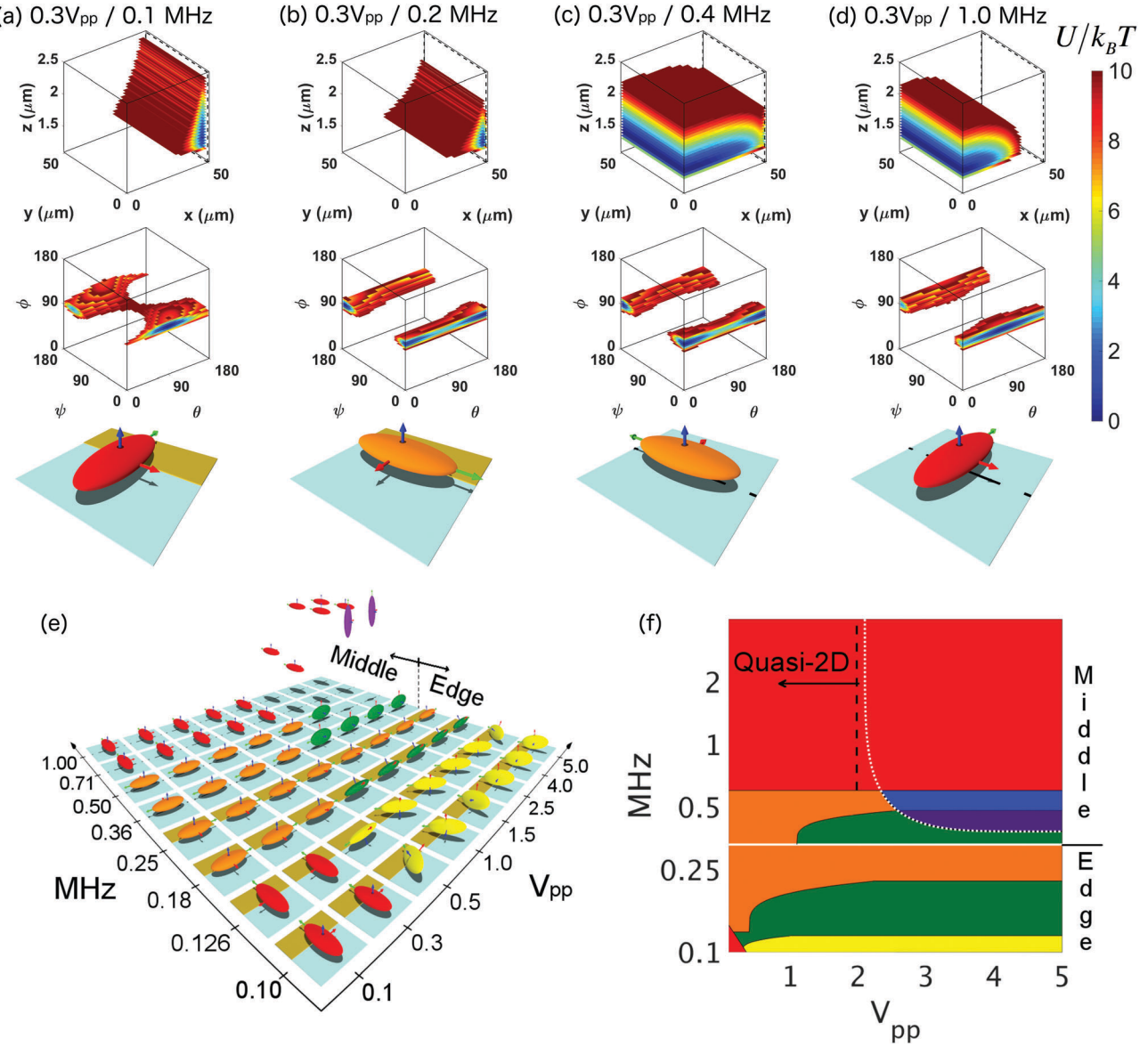

Fig. 5 Position and orientation projected energy landscapes for scalene ellipsoids ($r_x : r_y : r_z$ = 2 : 1 : 5) from 0–10 k_BT relative to the global energy minimum. Field conditions are for 0.3 V_{pp}, and frequencies of (a) 0.1, (b) 0.2, (c) 0.4, and (d) 1.0 MHz. (bottom) The lowest energy state is rendered under energy landscape plots. Material parameters are listed in Table 1. Low dimensional energy landscape projections are shown In Fig. S3 and S4 (ESI†). (e) Discrete rendered states *vs.* voltage and frequency category axes. (f) Continuous state diagram *vs.* field strength and frequency. Solid white line indicates the transition in position from the electrode edges to electrode center. Dashed white line indicates when particles move away from the surface. Dashed black line is maximum *V* for quasi-2D analysis (eqn (24)).

shows that the long axis of the particle is oriented parallel to the *x*-component of the electric field, and the short axis is oriented perpendicular to the surface. This corresponds to the configuration shown in red depicted at the bottom of Fig. 5(a).

Fig. 5(b) shows the projected 3D position and orientation landscapes at 200 kHz and 0.3 V_{pp}. Here, the particle center's most probable location is close to the edge of the electrode. The long axis of the particle is oriented perpendicular to the *x*-component of the field, and the short axis is oriented normal to the wall. For both 100 and 200 kHz, the f_{CM} has a positive value, which means that the particle is more polarizable than the surrounding medium, and located in the higher field region near the electrode edge. At 100 kHz the long axis is more polarizable than the short axis, but at 200 kHz the short axis is more polarizable than the long axis. At low fields, the ellipsoidal particle preferred orientation is correlated with the greater f_{CM} value; *i.e.* the axis of the particle that has the greater polarization will be oriented along the *x*-component of the field, and the shortest axis will be oriented perpendicular to the wall.

The projected 3D position and orientation landscapes at 0.3 V_{pp} and 0.4 MHz, and 1.0 MHz are shown in Fig. 5(c) and (d), respectively. At these conditions, the f_{CM} is negative, making the particle less polarizable than the medium to give a most probable location at the electrode gap center. From the projected

orientational landscape at 0.4 MHz (Fig. 5(c)), it is seen that the particle long-axis is oriented perpendicular to the *x*-component of the field with the short axis oriented normal to the wall. However, for higher frequencies, the orientation of the long axis of the particle changes to be parallel with the applied electric field. Even though in these cases the f_{CM} is negative, the orientation of the long axis is correlated to the higher polarization of the particle axis at every frequency. When the f_{CM} is negative, the absolute minimum of the energy landscape is located outside of the electrode gap on top of the electrode. However, an energy barrier located at the electrode edge practically keeps particles within the electrode gap. As such, our analysis is for particles at this local minimum, which is practically useful for manipulating particles within the electrode gap region.

Under this field strength (0.3 V_{pp}), the particle can be oriented in the same two orientational states at the electrode edge and the electrode center like prolate particles. The characteristic dipole–field interaction energy (λ = 0.8) is significantly less than the characteristic gravitational potential energy (G = 20, eqn (22)). This causes to the particle short-axis to always be aligned perpendicular to the surface. Eqn (24) predicts that a voltage <1.33 V_{pp} is required to maintain quasi-2D conditions. Even though the f_{CM} of the short axis has a larger value between 150 and 200 kHz, the applied voltage is not enough to rotate the particle to different orientational states.

To determine the maximum number of states for particles under different field conditions and medium conductivities, we repeat the analysis described in Fig. 3 and 4 for many energy landscapes *vs.* applied voltage (electric field) and frequency. Fig. 5(f) shows the equilibrium position and orientation of a scalene ellipsoid ($r_x : r_y : r_z$ = 2 : 1 : 5 μm). Fig. 5(e) depicts some representative voltage and frequency values of the entire analyzed spectrum, which is shown in Fig. 5(e) as a state diagram. The color scheme corresponds to the orientations and scheme in Fig. S2 (ESI†). Fig. 5 shows how the particle's orientation depends on voltage and frequency. As explained previously, at low voltages the particle short axis stays perpendicular to the wall allowing two orientational states at the electrode edge and two in the electrode gap center. As the voltage increases, particles realize different orientations since the dipole–field interaction energy along the *z*-axis (in the lab coordinate) becomes comparable to the gravitational energy as predicted by eqn (22) (*i.e.* the equilibrium position shifts to higher elevations). For a scalene particle, equilibrium states are reached when any of the particle axes is aligned perpendicular to the wall (Fig. 5(f)), which depends on the f_{CM} and applied voltage, or the polarization along the different particle axes.

At low frequencies, the particle is more polarizable than the surrounding medium and is located at the electrode gap edge. Here, it has four orientational configurations. Two of these states correspond to the long axis aligned and two of them perpendicular to the *x*-component of the field. Under these conditions, the short axis of the particle could be parallel or perpendicular to the wall. At high frequencies, the particle is located in the middle of the electrode gap. Here, we can distinguish five different orientational states, where the short axis is parallel in two of them and perpendicular to the wall in the others. The long axis is aligned parallel and perpendicular to the *x*-component of the field, and it can also be oriented normal to the surface. The predicted voltage (eqn (24)) for the quasi-2D threshold at high frequencies is represented as a dashed black line in Fig. 5, which is consistent with the particle orientations obtained from the most probable states in the energy landscapes.

Generality of energy landscapes

Based on the analysis in Fig. 3–5 and result in eqn (24), quasi-2D behavior is generally observed only at low field strengths. In particular, for applied voltages $<V_{pp,max}$ in eqn (24), the results in Fig. 3–5 show that the f_{CM} can predict the most probable position and orientation of dielectric ellipsoids at different frequencies. This finding shown that the axis with the highest polarization is aligned with the *x*-component of the field. In all of these cases the gravitational energy causes the short axis to be perpendicular to the underlying wall under low field strengths, so the particle orientation is defined by the f_{CM} of the remaining two axes.

The present analysis shows results for ellipsoidal particles with different aspect ratios, corresponding to prolate ($r_x : r_y : r_z$ = 2 : 1 : 5 μm), oblate ($r_x : r_y : r_z$ = 5 : 1 : 5 μm), and scalene ($r_x : r_y : r_z$ = 2 : 1 : 5 μm). The equations reported here are valid for arbitrary ellipsoidal particle shapes, including spheres. Our results show the main phenomenological characteristics of the position/orientation projected energy landscape for ellipsoidal particles, and the analytical description can be used to predict the behavior for different electrode configurations, such as spiral electrodes,[31] parallel plate electrodes,[13,32,33] quadrupole or octupole electrodes,[34] and others.[35,36] The behavior and number of positional and orientational states in every case depend on the f_{CM} and the relative components of the field in the laboratory coordinates. However, particles under the influence of non-uniform fields with azimuthal symmetry[31,36] will have a similar behavior along the radial direction as our present results. For parallel plate electrodes, the field is uniform and perpendicular to the plates, so the particle behavior is only limited by the gravitational energy, which results in two and three states for uni-axial and tri-axial particles. As such, our results are perhaps most useful for non-uniform AC electric fields with spatially varying gradients that produce local maxima and minima with frequency dependent orientations.

Here we list assumptions, limitations, and issues that might arise when comparing the models here with direct experimentally accessible information. The model here is based on uniform polarizable anisotropic ellipsoids at each position and orientation. This is a valid assumption if the particle size is smaller than the characteristic dimension of the field gradient. In the parallel electrode configuration, field gradients along the *x*-direction are greater at the edge of the electrode, which can generate an underestimation of the potential well at those locations (by neglecting higher multi-poles that have finite contributions[37]). Our results include analytical results for the particle position and orientation based on material and geometric properties of particle and the surrounding medium. However, in experiments, it is not necessarily a simple task to estimate conductivities along

particle axes. In future work, we plan to report how such parameters can be obtained by fitting optical microscopy measurements of energy landscapes *vs.* field frequency and amplitude to the expressions reported in this work.

Conclusions

Analytical expressions are reported for the time-average energy landscapes of prolate, oblate, and scalene ellipsoids in non-uniform AC electric fields between coplanar electrodes. Ellipsoid particle equilibrium positions and orientations are obtained from global minima of net potential energy landscapes computed from superposition of dipole-field, gravity, and ellipsoid-substrate electrostatic repulsion. This analysis yields the maximum number of possible states for ellipsoidal particles *vs.* field frequency and amplitude for the coplanar electrode configuration. Results indicate up to 9 states for scalene ellipsoids (4 orientations at field maximum, 5 orientations at field minimum), 6 states for prolate ellipsoids (3 orientations at field maximum, 3 orientations at field minimum), and 5 states for oblate ellipsoids (2 orientations at field maximum, 3 orientations at field minimum). To facilitate comparisons with experiments, a criterion is reported for the highest voltage or electric field, when particles can be reliably analyzed as quasi-2D (thermally sampled degrees of freedom are within a plane adjacent to underlying substrate). The analytical potential energy landscapes reported in the paper are general and can be used with different electrode geometries and electric field shapes.

Conflicts of interest

There are no conflicts to declare.

Acknowledgements

We acknowledge financial support by the National Science Foundation (CBET-1434993).

References

1 D. G. Grier, *Nature*, 2003, **424**, 810–816.
2 A. Ramos, H. Morgan, N. G. Green and A. Castellanos, *J. Electrost.*, 1999, **47**, 71–81.
3 C. Gosse and V. Croquette, *Biophys. J.*, 2002, **82**, 3314–3329.
4 J. V. I. Timonen and B. A. Grzybowski, *Adv. Mater.*, 2017, **29**, 1603516.
5 J. Fu, Q. Zhan, M. Y. Lim, Z. Li and H. D. Ou-Yang, *Opt. Lett.*, 2013, **38**, 3995–3998.
6 A. C. H. Coughlan and M. A. Bevan, *Phys. Rev. E*, 2016, **94**, 042613.
7 T. B. Jones, *Electromechanics of Particles*, Cambridge University Press, Cambridge, 1995.
8 H. Morgan and N. G. Green, *AC electrokinetics: colloids and nanoparticles*, Research Studies Press, Philadelphia, PA, 2003.
9 J. J. Juarez and M. A. Bevan, *J. Chem. Phys.*, 2009, **131**, 134704.
10 J. J. Juarez, J.-Q. Cui, B. G. Liu and M. A. Bevan, *Langmuir*, 2011, **27**, 9211–9218.
11 J. J. Juarez, B. G. Liu, J.-Q. Cui and M. A. Bevan, *Langmuir*, 2011, **27**, 9219–9226.
12 J. P. Singh, P. P. Lele, F. Nettesheim, N. J. Wagner and E. M. Furst, *Phys. Rev. E: Stat., Nonlinear, Soft Matter Phys.*, 2009, **79**, 050401.
13 A. A. Shah, H. Kang, K. L. Kohlstedt, K. H. Ahn, S. C. Glotzer, C. W. Monroe and M. J. Solomon, *Small*, 2012, **8**, 1551–1562.
14 A. Kuijk, T. Troppenz, L. Filion, A. Imhof, R. van Roij, M. Dijkstra and A. van Blaaderen, *Soft Matter*, 2014, **10**, 6249–6255.
15 S. J. Boehm, L. Lin, K. Guzmán Betancourt, R. Emery, J. S. Mayer, T. S. Mayer and C. D. Keating, *Langmuir*, 2015, **31**, 5779–5786.
16 M. Saito, H. P. Schwan and G. Schwarz, *Biophys. J.*, 1966, **6**, 313–327.
17 R. D. Miller and T. B. Jones, *Biophys. J.*, 1993, **64**, 1588–1595.
18 J. A. Stratton, *Electromagnetic Theory*, McGraw-Hill Book Company, Inc., New York, 1941.
19 I. Torres-Diaz and M. A. Bevan, *Langmuir*, 2017, **33**, 4356–4365.
20 L. R. White, *J. Colloid Interface Sci.*, 1983, **95**, 286–288.
21 P. Schiller, S. Krüger, M. Wahab and H. J. Mögel, *Langmuir*, 2011, **27**, 10429–10437.
22 D. J. Evans, *Mol. Phys.*, 1977, **34**, 317–325.
23 H. Morgan, A. García Izquierdo, D. Bakewell, N. G. Green and A. Ramos, *J. Phys. D: Appl. Phys.*, 2001, **34**, 1553–1561.
24 S. Singh, *Liquid Crystals: Fundamentals*, World Scientific, River Edge, NJ, 2002.
25 M. P. Lettinga, E. Barry and Z. Dogic, *EPL*, 2005, **71**, 692.
26 Y. Han, A. M. Alsayed, M. Nobili, J. Zhang, T. C. Lubensky and A. G. Yodh, *Science*, 2006, **314**, 626–630.
27 M. A. Bevan and S. L. Eichmann, *Curr. Opin. Colloid Interface Sci.*, 2011, **16**, 149–157.
28 D. Rossi, J. H. Han, W. Jung, J. Cheon and D. H. Son, *ACS Nano*, 2015, **9**, 8037–8043.
29 H. Brenner, *J. Colloid Interface Sci.*, 1981, **80**, 548–588.
30 H. Morgan and N. G. Green, *J. Electrost.*, 1997, **42**, 279–293.
31 X. B. Wang, Y. Huang, X. Wang, F. F. Becker and P. R. Gascoyne, *Biophys. J.*, 1997, **72**, 1887–1899.
32 B. W. Kwaadgras, T. H. Besseling, T. J. Coopmans, A. Kuijk, A. Imhof, A. V. Blaaderen, M. Dijkstra and R. V. Roij, *Phys. Chem. Chem. Phys.*, 2014, **16**, 22575–22582.
33 M. Suga, A. Kunimoto and H. Shinohara, *Biosens. Bioelectron.*, 2017, **97**, 53–58.
34 Y. Huang and R. Pethig, *Meas. Sci. Technol.*, 1991, **2**, 1142.
35 K. A. Collins, X. Zhong, P. Song, N. R. Little, M. D. Ward and S. S. Lee, *Langmuir*, 2015, **31**, 10411–10417.
36 J. J. Crassous and A. F. Demirors, *Soft Matter*, 2017, **13**, 88–100.
37 E. Liang, R. L. Smith and D. S. Clague, *Phys. Rev. E: Stat., Nonlinear, Soft Matter Phys.*, 2004, **70**, 066617.

